JTTEE5 12:492-503

A Computational Fluid Dynamic Analysis of Gas and Particle Flow in Flame Spraying

Robi Bandyopadhyay and Per Nylén

(Submitted 15 December 2001; in revised form 29 October 2002)

The flame spraying process, which is a common industrial thermal spraying application, has been analyzed by means of three-dimensional computational fluid dynamics (CFD) simulations. The process used at the Volvo Aero Corporation for the coating of fan and compressor housings has been modeled. The process uses the Metco 6P torch (Metco, Westbury, NY), which ejects a mixture of acetylene and oxygen at high speed through a ring of 16 orifices to form the flame. A stream of argon gas flowing through an orifice in the center of the ring carries a powder of nickel-covered bentonite through the flame to the spray substrate. The torch is cooled by a flow of air through an outer ring of 9 orifices. The simulation emulated reality closely by including the individual inlets for fuel, cooling air, and injected particles. The gas combustion was simulated as a turbulent, multicomponent chemically reacting flow. The standard, two-equation k-ε turbulence model was used. The chemical reaction rates appeared as source terms in the species transport equations. They were computed from the contributions of the Arrhenius rate expressions and the Magnussen and Hjertager eddy dissipation model. The first simulations included several intermediate chemical substances whose predicted concentration agreed favorably with measurements. Later, more simplified simulations incorporated only the global chemical reaction involving the initial and the final products, with corrections to the thermal properties being made to account for the missing intermediaries. The gas velocity and temperature fields predicted by the later simulations compared satisfactorily to those predicted by the earlier, more elaborate, ones. Therefore, the final simulations, which incorporated injected particles, were conducted employing the simplified model with only the global reaction. An in-house finite difference code was developed to calculate particle properties. Allowance was made for elliptical shapes, phase changes, and internal heat transfer with regard to the composite material. The particle velocities and temperatures predicted by the final simulations compared fairly well with experimental results obtained with the optical DPV2000 system.

Keywords chemical species, computational fluid dynamics, flame spraying, modeling, particle flow

1. Introduction

Flame spraying is a common thermal spraying process in which the spray material is transported by a carrier gas (in this case argon) and is heated through a flame of burning gases (in this case acetylene and oxygen). The gas and particle velocities in flame spraying are commonly much lower than those achieved by plasma and HVOF spraying torches. The low particle velocities, typically 15-30 m/s, produce low density porous coatings. An example of such a coating is the nickel-chromium/bentonite layer sprayed on the mating parts of the shovel tops of fan blades and on the inside of compressor housings, to reduce losses due to airflow in aircraft engines.

The combustion of premixed acetylene/oxygen in flame spraying produces temperatures in the range of 3000-3400 K, as compared with typical temperatures of over 10 000 K in plasma spraying. As the local flame temperature is close to both the melting and boiling points for the coating material (e.g., in the case of nickel 1726 K and 3110 K, respectively), the result is very sensitive to any variations of the process parameters. If, for instance, the mixing ratio is slightly changed, the flame temperature will also change, causing in turn a significant change to the coating structure and its properties. The optimization of the process by practical experimentation has proved to be both difficult and expensive. The prediction of gas and particle flow fields by the use of simulations may make it possible to optimize spraying conditions and gain control over particle properties before impact and thereby regulate the quality of a coating. Due to the need for such a simulation tool, a research program was started at the University of Trollhättan/Uddevalla in collaboration with the Volvo Aero Corporation (Trollhättan, Sweden) to develop a model for the process using computational fluid dynamics (CFD). The initial efforts, though unsuccessful, revealed the complexity of the problem and led to the refinement of both soft- and hardware. Subsequent attempts, made since the later half of 1999, have used a powerful commercial software package (FLUENT 5.5, Fluent Inc., Lebanon, NH) in conjunction with a locally developed cluster of ten twin 800 MHz workstations.

A number of papers have been presented which have analyzed the closely related HVOF process,[1-7] including recently published three-dimensional CFD-analyses with a full coupling between particle and gas flow through momentum and energy exchanges.[5] However, at the present time, the low velocity oxygen fuel (LVOF) process does not yet appear to have been modeled. Many empirical parametric studies have been performed without a detailed understanding of the physical and chemical processes involved. In this article, a three-dimensional simulation with full coupling between the particle and gas flows

---

Robi Bandyopadhyay and **Per Nylén**, University of Trollhättan/Uddevalla (HTU), Box 957, S-461 29, Trollhättan, Sweden. Contact e-mail: robi@htu.se.

Nomenclature

D	particle diameter (m)
R	radial co-ordinate (m)
A	particle radius (m)
K	turbulent kinetic energy in the k-ε law
E	dissipation rate of k in the k-ε law
$k_{f,k}$ and $k_{b,k}$	forward and backward rate constants in the Arrhenius rate expressions
A_k	preexponential factor (consistent units)
β_k	temperature exponent (dimensionless)
E_k	activation energy for the reaction (J/kmol)
R	universal gas constant (J/kmol-K)
T	local temperature (K)
$\text{grad}T_{Ni}$	local temperature gradient in the nickel alloy coating of the injected particles (K)
$\text{grad}T_{Be}$	local temperature gradient in the bentonite core of the injected particles (K)
δT	temperature change (K)
T_f	local fluid temperature (K)
T_a	local temperature at the particle surface (K)
T_8	ambient temperature (K)
T_{Mni}	melting point of Nickel (K)
L_m	latent heat of melting for Nickel (JKg^{-1})
λ	thermal conductivity [J/(mK)]
λ_{Ni}	thermal conductivity of Nickel alloy [J/(mK)]
λ_{Be}	thermal conductivity of Bentonite core [J/(mK)]
q	transferred heat (J)
h	heat transfer coefficient (J/K)
κ_f	conductivity of the fluid at the local fluid temperature [W/(mK)]
Re	Reynolds number
Nu	Nusselt number
Pr_w	Prandtl number of the fluid at the surface temperature of the particle
Kn	Knudsen number
σ	Stephan-Boltzmann constant [$W/(m^2K^4)$]
ε_p	emissivity of the particle
γ	specific heat ratio
ρ	density (kg/m^3)
ρ_f	density of the fluid at the local fluid temperature (kg/m^3)
ρ_w	density of the fluid at the wall temperature of the particle (kg/m^3)
ν	kinematic viscosity [$m^4/(kgs)$]
μ	viscosity (Ns)
μ_f	viscosity of the fluid at the local fluid temperature (Ns)
μ_w	viscosity of the fluid at the wall temperature of the particle (Ns)
c_p	specific heat [J/(kgK)]
c_{pp}	particle specific heat [J/(kgK)]
f	correction factor (dimensionless)

Acronyms

HVOF	High velocity oxygen fuel
LVOF	Low velocity oxygen fuel
CFD	Computaional fluid dynamics
VAC	Volvo Aero Corporation
HTU	University of Trollhättan/Uddevalla
lpm	liters per minute
gpm	grams per minute
2-D	two dimensional (refers to geometry)
3-D	three dimensional (refers to geometry)

of a chemically reacting flow in a commercial flame-spraying torch is presented and compared with measurements. The objective was not only to create a successful simulation of the process, but also to produce a working model, which can be used for parameter studies between spray gun parameters and particle in-flight characteristics. Thus, individual inlets for the fuel, for the air, and for the particles were therefore considered. Furthermore, turbulence, multicomponent gas flows, as well as the numerous chemical reactions, have all been taken into consideration, and an in-house developed code for calculating internal heat transfer has been created.

2. The Process Model

Figure 1 shows a representation of the process. The cooling air is injected through an outer ring of orifices. The fuel gases, C_2H_2 and O_2, are premixed and injected through a ring of 16 orifices around the nozzle rim, while the powder is transported by argon through the axial orifice. The diffusion combustion of the fuel extends in a free jet transporting the particles to the substrate located about 20 cm from the nozzle exit. For the purpose of this article, a region of space encompassing the free jet region in front of the nozzle, where the heating and acceleration of the particles occurs, was selected for modeling. This region was 0.241 m in length and 0.056 m in diameter. The size of the modeled region was determined empirically to satisfy the conflicting needs of computational accuracy and economy. To verify the choice of diameter for the control volume, test simulations were performed on a wider region (diameter 0.508m).

For computational economy, the symmetry of the process geometry was utilized to concentrate the investigation on a wedge-shaped segment encompassing 1/8th of the cylindrical region (Fig. 2).

The interior of the investigated segment was assumed to contain a fluid material composed of a mixture of reacting gases. The turbulent gas flow was modeled using the standard k-ε model.[8] It is a semi-empirical model based on two transport equations for the turbulent kinetic energy (k) and its dissipation rate (ε). In the derivation of the k-ε model, it was assumed that the flow is fully turbulent, and the effects of molecular viscosity are negligible. The choice of this turbulence model also enables the use of the eddy-dissipation model as a competing mechanism for species creation/destruction, together with the Arrhenius finite-rate mechanism, which is described in the "Chemical Reactions" section below.

The stepped end boundary (adjacent to the torch) of the segment consists of the nozzle and an outer ring of surrounding air. The nozzle is modeled as an adiabatic solid surface. The nozzle

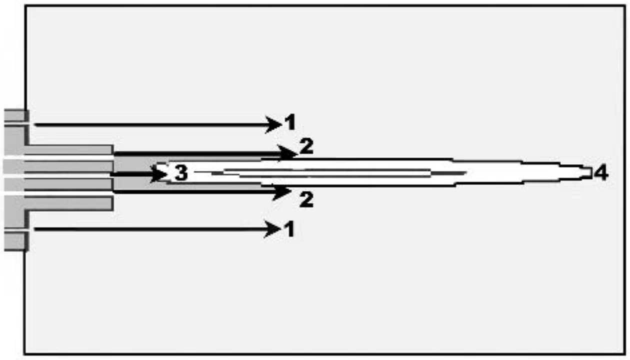

Fig. 1 Scheme of the flame spray process (1: cooling air through outer ring of 9 orifices at 200 m/s, 2: premixed C_2H_2/O_2 through inner ring of 16 orifices at 117 m/s, 3: argon carrier gas at 12 m/s, 4: spray substrate)

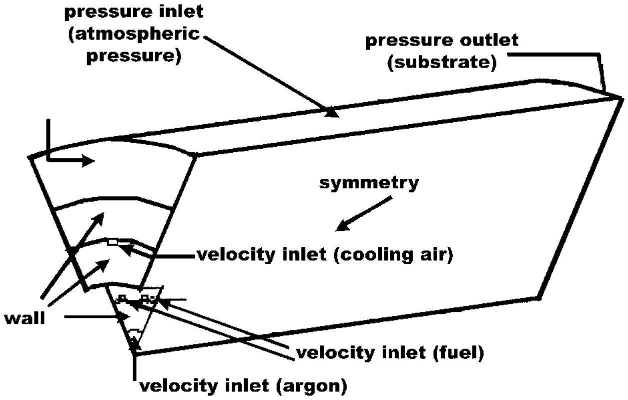

Fig. 2 The segment investigated and boundary conditions, showing two fuel inlet holes and one cooling air inlet

Table 1 Parameters Held Constant in the Simulation

Parameter	Value
Atmospheric pressure	1.01325 bar
Environmental temperature	300 K
Inlet temperature	300 K

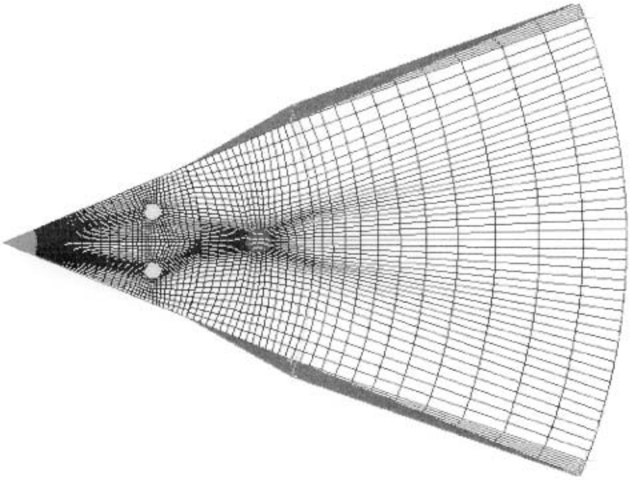

Fig. 3 The computational grid for both multi- and single-reaction simulations. The inlet end is viewed from the nozzle, showing a segment of the axial powder port, two fuel inlets, and one cooling air inlet.

is pierced by an inlet hole for the argon carrier gas at the center, two fuel inlet holes (which appear in the segment, out of the total of 16 in the nozzle) near the inner rim (the "lower step") and one hole for the cooling air toward the outer periphery (the middle of the "upper step") (Fig. 2).

The stream of argon carrier gas is modeled as a one-component steady flow at 12.6 m/s, corresponding to 6 lpm. The fuel/air mixture enters through the fuel inlets at 117.4 m/s, corresponding to 22.9 lpm of acetylene and 32 lpm of oxygen. The cooling air enters at 200 m/s, which was determined by a separate simulation based on the process geometry and a gauge pressure of 2 bars.

The part of the stepped end outside of the nozzle has boundary conditions corresponding to the free atmosphere (pressure inlets at zero gauge pressure). The same applies to the outer, lateral wall of the wedge. The two sides of the wedge separating it from the rest of the cylinder have symmetrical boundary conditions, implying that there are zero gradients of pressures and velocities across them. The other plane end of the wedge has free atmospheric exit conditions (pressure outlet at zero gauge pressure).

The particle injections, where applicable, were introduced as a surface injection, spread out uniformly over the argon orifice. The powder flow corresponds to 17.5 gpm. The particles escape at the substrate end.

The atmospheric conditions were modeled by keeping the parameters shown in Table 1 constant.

3. The Meshing of the Computational Region

The defined geometry was discretisized by using a mesh of computational cells, collected in a grid. GAMBIT 1.2, a companion program for FLUENT, was used to model and mesh the computational region. The meshing was found to be of crucial importance for the practical applicability of the model. Many different meshes were attempted on the same geometry, which included length scales between 0.008 m (diameter of a fuel inlet orifice) and 0.2413 m (length of the computational region). If the mesh created was too coarse, the shear layers of the flame were not resolved and the solutions were either divergent or incorrect. If, however, the mesh was too fine, the solution took a very long time to converge. The broad range of the length scales made it necessary to include some cells with highly flattened or elongated forms that can be the source of potential errors. The number of such oblong cells could be minimized but not entirely eliminated, and much time was spent on mesh refinement.

Close to the individual fuel and air inlets, grid clustering was needed (Fig. 3, 4). The grid was progressively refined. Starting with a coarse initial grid, partial solutions were obtained, which were used for finer meshing of the regions of high field gradi-

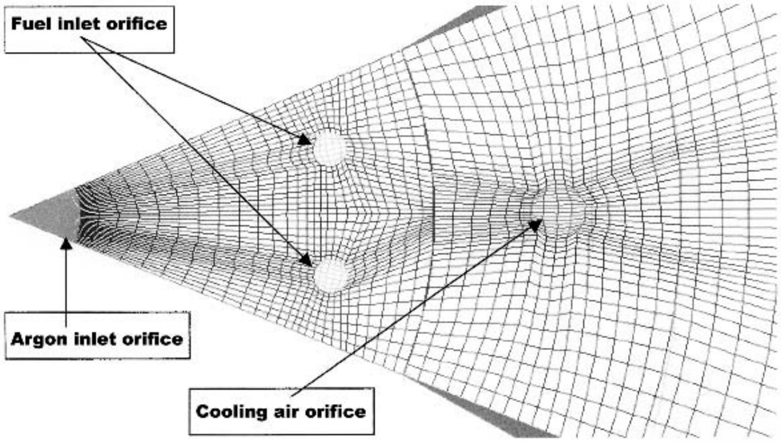

Fig. 4 A closer view of the mesh shown in Fig. 3, showing meshes of the fuel and air orifices

ents, until convergence was obtained. Thereafter, it was further refined until convergence was obtained quickly and with a minimum of computational effort.

For example, in the axial direction, a grid of 60 nodes led to divergence, because after a successful initial development, the flame could not be resolved in the high gradient regions close to the nozzle. With 80 or more axial nodes, convergence could be obtained. The final mesh incorporated 100 axial nodes.

Comparing the values of selected predictions from simulations with different degrees of grid refinement tested grid sensitivity. Grid sensitivity trials were made by subsequently increasing the number of nodes. The grid was considered to be sufficiently refined when two sets of computed results for two successive grid configurations differed by no more than 1%. The final number of nodes was 261 272.

4. The Computation

Three computational models were used for this article. The first one involved detailed chemistry and numerous chemical reactions, and is henceforth called the "multireaction model." The second model resembled the first in all aspects, including the meshing, except that the multitude of reactions was replaced by one global reaction and modified material properties, and is henceforth referred to as the "single-reaction model." The developed particle model was also integrated into this model. The third model was a two-dimensional, axis-symmetric simulation using the "single-reaction model," performed on a volume of a larger radial extent (0.508 m). This axis-symmetric calculation was performed to verify that the initial pressure boundary condition was not set too close to the flame.

For the current simulation involving heat exchange and viscous flows, energy exchange was included among the governing equations, and the standard k-ε model for turbulence (see below) was selected for the viscous fluids. The fluid within the control volume was assumed to be a mixture of compressible, ideal gases. The number of gaseous species was set at 15 for the multireaction model and 6 for the single-reaction model. The temperature field was not known at the outset, but was "ignited" by assuming a starting temperature of 1000 K throughout the control volume.

5. Chemical Reactions

As the process involves chemical reactions and fast moving, turbulent gas flows, a generalized finite rate formulation was applied. This approach is based on the solution of the species transport equations for reactants and product concentrations, based on the chemical reaction mechanism defined for the problem. The reaction rates influence the rate of creation/destruction of a species, which appears as a source term in the species transport equations. These rates were computed from the Arrhenius rate expressions or by using the eddy dissipation concept as used by Magnussen and Hjertager (a process that involves two quantities k and ε, see below), whichever is locally dominating or slower. Brief descriptions of these two concepts and their applicability are given below.

In the Arrhenius concept, the rate of creation/destruction of a species can be computed using an expression that requires user inputs for calculating the forward and backward rate constants $k_{f,k}$ and $k_{b,k}$ for a reaction k where the species participates. These constants are in turn then computed using the Arrhenius expression.

$$k_{f,k} = A_k T^{\beta_k} \exp(-E_k/RT) \qquad \text{(Eq 1)}$$

where A_k denotes the preexponential factor (consistent units), β_k denotes the temperature exponent (dimensionless), E_k denotes the activation energy for the reaction (J/kmol), and R denotes the universal gas constant (J/kmol-K). The Arrhenius expression for species creation/destruction rates is applicable when turbulence is not the dominating mechanism.

In the Magnussen and Hjertager eddy-dissipation concept, the rates of species of creation/destruction are calculated using the dominant of the two expressions, in which the turbulent kinetic energy (k) and its dissipation rate (ε) participate. The model is useful for the prediction of premixed and diffusion problems as well as for partially premixed reacting flows.

In turbulent reacting flows, each equation is calculated by FLUENT using the Arrhenius reaction rate, the eddy-dissipation-model reaction rate, or both, depending on the problem definition. If both are calculated, the limiting (slowest) rate is used as the reaction rate, and the contributions to the source terms in the species conservation and energy equations are calculated from this reaction rate. This was the approach selected for the current simulations, as empirically, it was found to produce the most realistic results.

The data for the global or overall reaction for combustion of the acetylene/oxygen mixture was provided by the FLUENT database as

$$2C_2H_2 + 5O_2 \rightarrow 4CO_2 + 2H_2O$$

5.1 Simulation With the Multireaction Model

The multireaction simulations used a number of intermediate chemical species to perform comparisons with the measurements conducted at VAC. The following fifteen species were included: C_2H_2, O_2, CO_2, H_2O, N_2, Ar, CO, H, H_2, HO_2, OH, O, N, NO, and N_2O. To calculate the concentrations of these substances, 22 reversible reactions were included Table 2). The reaction rates and Arrhenius constants were taken from published data.[8]

The data for the properties of the reactant species was taken from the FLUENT database, except for N, NO, and N_2O, where data from the JANAF[9] tables was used. FLUENT's data, where available, was verified against data in the JANAF tables.

5.2 Simulation With the Single-Reaction Model

The global reaction alone was used for the remainder of the simulations, including those with spraying particles. To allow for energy loss due to dissociation, the specific heat values of the chemical species were altered from those given in the JANAF tables to empirically determined values provided by Boulos et

Table 2 Defined Reactions

No.	Reaction	Preexponential Factor Consistent Units	Activation Energy, J/kmol	Temperature Exponent, Dimensionless
1	$O_2 + M \rightarrow 2O + M$	1.86 e 8	4.04 e 8	0.5
2	$2O + M \rightarrow O_2 + M$	37 150	−9.25 e 7	0
3	$2OH \rightarrow H_2O + O$	602 560	0	1.3
4	$H_2O + O \rightarrow 2OH$	2.138 e 11	8.46 e 7	0
5	$CO + O + M \rightarrow CO_2 + M$	3.236 e 7	−1.76 e 7	0
6	$CO_2 + M \rightarrow CO + O + M$	1.12 e 13	5.09 e 8	0
7	$CO + O_2 \rightarrow CO_2 + O$	2.51 e 9	2 e 8	0
8	$CO_2 + O \rightarrow CO + O_2$	3.31 e 10	2.29 e 8	0
9	$CO + OH \rightarrow CO_2 + H$	15 000	3 350 000	1.3
10	$CO_2 + H \rightarrow CO + OH$	9.77 e 10	1.07 e 8	0
11	$O + N_2 \rightarrow N + NO$	1.9 e 11	3.19 e 8	0
12	$N + NO \rightarrow O + N_2$	4.22 e 10	4 250 000	0
13	$N + O_2 \rightarrow NO + O$	1.129 e 7	2.783 e 7	1
14	$NO + O \rightarrow N + O_2$	2 400 000	1.62 e 8	1
15	$H_2 + M \rightarrow 2H + M$	2.24 e 9	3.88 e 8	0.5
16	$2H + M \rightarrow H_2 + M$	3.16 e 7	−4.44 e 7	0
17	$N + OH \rightarrow NO + H$	4.759 e 10	−5 230 000	0
18	$NO + H \rightarrow N + OH$	1.3 e 11	2.0585 e 8	0
19	$O_2 + H \rightarrow OH + O$	1.23 e 14	6.95 e 7	−0.9
20	$OH + O \rightarrow O_2 + H$	5.62 e 9	−7 540 000	0
21	$O + H_2 \rightarrow OH + H$	1.82 e 7	3.68 e 7	1
22	$OH + H \rightarrow O + H_2$	2.4 e 10	3.73 e 7	0
23	$H_2 + OH \rightarrow H_2O + H$	1 200 000	1.5 e 7	1.3
24	$H_2O + H \rightarrow H_2 + OH$	1.9 e 11	9.1 e 7	0
25	$H + OH + M \rightarrow H_2O + M$	7.586 e 17	0	−2.6
26	$H_2O + M \rightarrow H + OH + M$	1.35 e 13	4.78 e 8	0
27	$O_2 + H + M \rightarrow HO_2 + M$	2 e 12	0	−1
28	$HO_2 + M \rightarrow O_2 + H + M$	1.07 e 12	1.876 e 8	0
29	$HO_2 + H \rightarrow 2OH$	2.51 e 11	7 955 000	0
30	$2OH \rightarrow HO_2 + H$	1.78 e 10	1.78 e 8	0
31	$HO_2 + O \rightarrow O_2 + OH$	4.786 e 10	4 190 000	0
32	$O_2 + OH \rightarrow HO_2 + O$	5.25 e 10	2.36 e 8	0
33	$HO_2 + H \rightarrow O_2 + H_2$	3.02 e 10	2 930 000	0
34	$O_2 + H_2 \rightarrow HO_2 + H$	7.07 e 10	2.43 e 8	0
35	$HO_2 + OH \rightarrow H_2O + O_2$	5.01 e 10	4 200 000	0
36	$H_2O + O_2 \rightarrow HO_2 + OH$	6.026 e 11	8.09 e 8	0
37	$N_2O + M \rightarrow N_2 + O + M$	5.37 e 11	2.36 e 8	0
38	$N_2 + O + M \rightarrow N_2O + M$	1.41 e 7	8.16 e 7	0
39	$N_2O + O + M \rightarrow N_2 + O + M$	1.66 e 10	8.65 e 7	0
40	$N_2 + O + M \rightarrow N_2O + O + M$	1.02 e 10	4.29 e 8	0
41	$N_2O + O \rightarrow 2NO$	2 e 10	9.085 e 7	0
42	$2NO \rightarrow N_2O + O$	5.75 e 8	2.51 e 8	0
43	$N_2O + H \rightarrow N_2 + OH$	8.91 e 10	6.49 e 7	0
44	$N_2 + OH \rightarrow N_2O + H$	4.365 e 9	3.395 e 8	0

M denotes a catalytic reactant (third body) al.[10] For example, the values of the specific heat for O_2 are shown in Fig. 5.

6. The Particle Model

The powder particles used in this study are composed of nickel-chromium-aluminum and leached stabilized bentonite clay according to the weight specification shown in Table 3.

Based on this specification, the composition shown in Table 4 was assumed for the modeled particles.

The particles are highly asymmetrical in form,[11] with a metal coating of varying thickness covering the bentonite core. The nonspherical form was accounted for by selecting FLUENT's nonspherical particle form with a shape factor of 0.1. Table 5 gives the size distribution of the particles.

Based on the above specification, the size distribution shown in Table 6 was assumed for the modeled particles.

The size distribution assumed in Table 6 implies the approximate diameter distribution shown in Table 7.

The metal coating of the composite particles undergoes melting and some of the constituents are vaporized. For the current simulations, two models of the injected particles were used. The first was a lumped model, where the particle's density, specific heat, and thermal conductivity were assumed to be the weighted average of those of its constituent materials. For this model, the latent heat of melting and boiling of the nickel coating were accounted for by increasing the specific heat of the particle over a short (2 K) temperature interval.

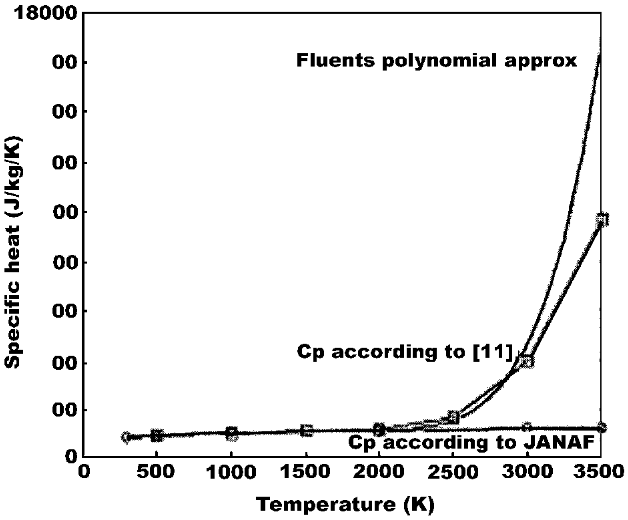

Fig. 5 Specific heat of O_2 as a function of temperature

The lumped model was found to yield unsatisfactory predictions of particle temperatures. The surface conductivity of this model, being the weighted average of the conductivity of nickel and bentonite, was too low to allow sufficient heat into the particle, which in turn resulted in unacceptably low particle temperatures. The melting temperature of nickel was seldom reached, and the physical process was therefore incorrectly represented. A model considering internal heat transfer was therefore developed. In this model, the particle was assumed to be somewhat elliptical, with a core of bentonite and a surface layer of NiCrAl, according to the specifications. The transfer of heat from the fluid to the particle surface was assumed to take place in accordance with Newton's law of heating.

$$\lambda\left(\frac{\delta T}{\delta r}\right)_{r=a} = q \qquad \text{(Eq 3)}$$

where λ is the thermal conductivity of the particle surface, T is the particle temperature, r = a indicates that the equation applies at the particle's surface and the heat transfer, q, between the fluid and particle surface given by

Table 3 Particle Composition Specification

Component	wt.%
Ni	63-73%
Stabilized bentonite	18.0-24.5%
Al	2.3-6.1%
Cr	2.3-5.5%
Others	Max 4.0%

Table 4 Modelled Particle Composition

Component	wt.%
Ni	70%
Bentonite	22%
Al	5%
Cr	3%

Table 5 Particle Size Specification

Retained on Sieve, Mesh, µm	Passing Sieve, Mesh, µm	wt.%
300		Max 0.5
150		Max 2
106		15-30
75	106	40-70
	75	15-30
	45	Max 5

Table 6 Modelled Particle Size Distribution

Diameter Range, µm	wt.%
10-50	5
50-80	25
80-130	48
130-200	20
200-330	2

Table 7 Numeric Proportion of Particles Within Diameter Ranges

Diameter Range, µm	Number in Percent
10-50	46
50-80	32
80-130	19
130-200	3
200-300	0.1

$$q = h(T_f - T_a) + \varepsilon_p \sigma(T_\infty^4 - T_a^4) \qquad \text{(Eq 4)}$$

where T_f is the local fluid temperature, T_a is the temperature at the particle surface, and T_8 the temperature of the surroundings. σ is the Stephan-Boltzmann constant, and ε_p is the particle's emissivity. The heat transfer coefficient h is given by

$$h = Nu\frac{\kappa_f}{d} \qquad \text{(Eq 5)}$$

where κ_f is the conductivity of the fluid at the local fluid temperature, d is the particle diameter, and Nu is the Nusselt number, which, for a medium of constant properties, may be calculated from the Ranz and Marshall equation[12]:

$$\mathrm{Nu} = 2.0 + 0.514\mathrm{Re}^{1/2} \qquad \text{(Eq 6)}$$

where Re is the Reynolds number. An alternative expression for Nu for a medium of constant properties is given by Lee et al.[13]:

$$\mathrm{Nu} = 2.0 + 0.6\mathrm{Re}^{1/2}\mathrm{Pr}^{1/3} \qquad \text{(Eq 7)}$$

where Pr is the Pranndl number.

On application, it was obvious that the heat transfer from the heated fluid to the particle according to Eq 3-6 was inadequate. Equation 6 and 7 assume constant properties of the fluid medium, while in reality there is a temperature difference of about 3000 K when a cold particle enters a hot flame, and again when a hot particle flies through a cooled gas medium; conditions that account for the larger part of the particle trajectory.

Several expressions for the Nusselt number that take account of the variable property effects are suggested in the literature.[13] Though they were presented for plasma spraying, the derivations could be applied to the effects of variable, temperature-dependent properties of any fluid medium and as such they should be applicable even for flame spraying. The correction proposed by Lewis and Gauvin[14] was the following expression (8), in the continuation known as the Lewis expression.

$$\begin{aligned}\mathrm{Nu} &= (2 + 0.515\mathrm{Re}_f^{1/2})(\nu_f/\nu_\infty)^{0.15} \\ &= (2 + .515\mathrm{Re}_f^{1/2})(\mu_f\rho_\infty/(\mu_\infty\rho_f))^{0.15} \qquad \text{(Eq 8)}\end{aligned}$$

where ν is the kinematic viscosity, μ is the viscosity, and ρ is the density, while the subscript f refers to the properties corresponding to the film temperature, and the subscript ∞ the properties corresponding to the free stream temperatures.

Lee et al.[13] proposed the expression (in the continuation called the Lee expression)

$$\mathrm{Nu}_f = (2 + 0.6\mathrm{Re}_f^{1/2}\mathrm{Pr}_f^{1/3})(\rho_\infty\mu_\infty/(\rho_w\mu_w))^{0.6}(c_{p_\infty}/c_{p_w})^{0.38} \qquad \text{(Eq 9)}$$

where c_p denotes the specific heat of the fluid, and the subscript w denotes the properties at the wall temperature of the particle.

The gas mixture properties were interpolated from Boulos et al.[10] and Gurvich et al.[15]

Within the particle, heat is transferred by conduction, which, assuming spherical symmetry, can be written

$$\rho c_{pp}\frac{\partial T}{\partial t} = \lambda\frac{1}{r^2}\frac{\partial}{\partial r}\left(r^2\frac{\partial T}{\partial r}\right) \qquad \text{(Eq 10)}$$

where ρ is the particle density, c_{pp} the particle specific heat, and λ the particle conductivity. While calculating the temperature changes for the elements located within the metal coating at the melting and boiling points of the metal, the corresponding latent heats were absorbed or emitted. When the temperature of an element of the metal coating reached the boiling point of nickel, any subsequent addition of heat led to depletion of that element by boiling. The model incorporated the successive mass reduction of the particle by the loss of the elements of the coating by boiling. The diameter of the particle was thus gradually reduced until only the bentonite core was left. At the boundary between the alloy and the core, the heat flow balance (Fourier's law) led to the relationship

$$\mathrm{gradT}_{Ni} * \lambda_{Ni} = \mathrm{gradT}_{Be} * \lambda_{Be} \qquad \text{(Eq 11)}$$

where λ symbolizes conductivity, gradT the gradient of the local temperature field, and the subscripts Ni and Be denote the materials nickel and bentonite, respectively. At that boundary, the two substances have the same temperature. At the center, the gradient of the temperature field is zero. Below the sintering temperature of bentonite, 1400 K, the material properties of the core were those of bentonite powder. Above the sintering temperature, they were those of the bulk material. Based on the above equations, the temperature field within the particle was calculated by the program. This model gave much insight into the details of the process.

Although the alloy accounted for the greater part of the weight of the particle, the high density of the alloy and the low density of the bentonite made the alloy layer relatively thin—only about 6% of the diameter of a spherical particle. The simulation predicted that at an early point in the flight path (after about 5-15 mm), the nickel coating reached the boiling point of nickel and evaporated, having heated the bentonite core to a high temperature. As the core had now crossed the sintering temperature of bentonite—about 1400 K—the thermal conductivity of the bentonite was increased from a lower value applicable for the powder material to the higher value corresponding to the bulk thermal conductivity of bentonite. This allowed it to absorb more heat from the flame and remain above the sintering temperature until reaching the substrate, so that it can adhere to the substrate and build the coating. At the same time, the diameter and mass of the particle is reduced, resulting in an increased velocity.

The presence of turbulence in the fluid was considered in the calculations of the particle trajectories. The injections were distributed over the entire inlet surface. At the wedge boundaries, where symmetrical boundary conditions apply, the particles are allowed to escape. No corresponding particles enter the wedge from the adjacent wedges, as would be the case in reality. If one particle escaped prematurely, it was injected again, until it flowed through the domain to the distance where the statistics were computed. The simulations were therefore considered to be truly three-dimensional.

7. Results and Discussion

7.1 Verification of the Multireaction Model: The Comparison of Predicted and Measured Gas Field Concentrations

The results of the 2-D simulation conducted on a wider region (see above section, "The Computation") agreed closely with those of the 3-D simulations, showing that the size of the domain chosen for the 3-D simulation was sufficient. The predictions of species concentrations were compared with corresponding values reported from IR, chemiluminescence, and paramagnetic measurements. The predicted and measured data sets (in mass fractions) are presented in Fig. 5-9. The measured lines are dotted, while the simulated are continuous. Each figure shows three lines, corresponding to values along the flame axis, at 1 cm (radial) and at 5 cm out from the axis. Each pair of measured and corresponding simulated lines carries the same symbol. The points correspond to axial distances of 5 cm, 10 cm, 15 cm, and 20 cm from the nozzle exit.

The O_2 concentrations (Fig. 6) indicate that the flame has a narrower and more tapered shape in the predictions in comparison with the measurements. The CO_2 concentrations (Fig. 7) tend to be lower for the predictions closer to the substrate, as is the case with the water vapor concentrations (Fig. 8). The concentrations of the traces of CO (Fig. 9) and NO (Fig. 10) agree closely in magnitude. A possible explanation for the apparent discrepancy in the length of the flame is the air cooling pressure. The simulations indicated that the shape of the flame is fairly sensitive to this pressure and, unfortunately, it was not recorded during the measurements.

The gas concentrations predicted by the simulations were found to agree fairly well with the measured values, and the differences had similar characteristics for all species, indicating a somewhat shorter and more intensive flame in the predictions. The overall conclusion after considering the five gas concentrations was that the multireaction model could be considered to be a successful simulation.

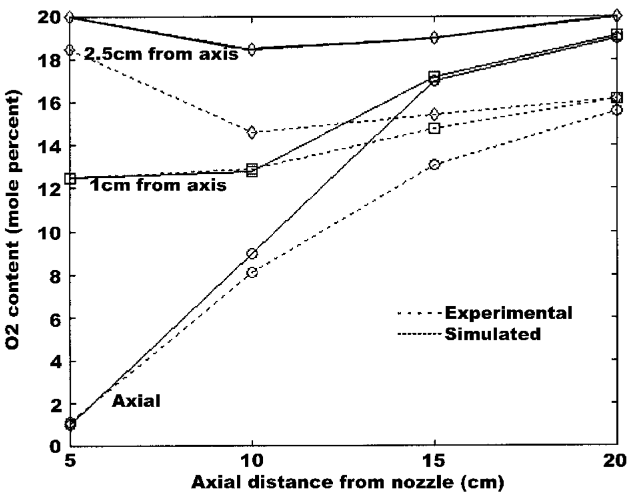

Fig. 6 Predicted and measured O_2 concentrations

7.2 Verification of the Single-Reaction Model: The Comparison of Temperature and Velocity Fields With the Multireaction Simulation

No experimental measurements of gas velocity and temperature fields were available, but gas velocity and temperature fields predicted by the single-reaction simulations were compared with those predicted by the multireaction model (Fig. 11, 12).

An overall conclusion that can be drawn from these comparisons is that the gas temperature and gas velocity fields produced by the two models agree quite closely. The influence of the gas flow on the inert coating particles occurs through the gas velocity and temperature fields. It was therefore considered justifiable to base simulations involving particle injections on the single-reaction model. The convergence time for the simulations without the reversible reactions was significantly shorter, taking only a number of hours instead of a number of days.

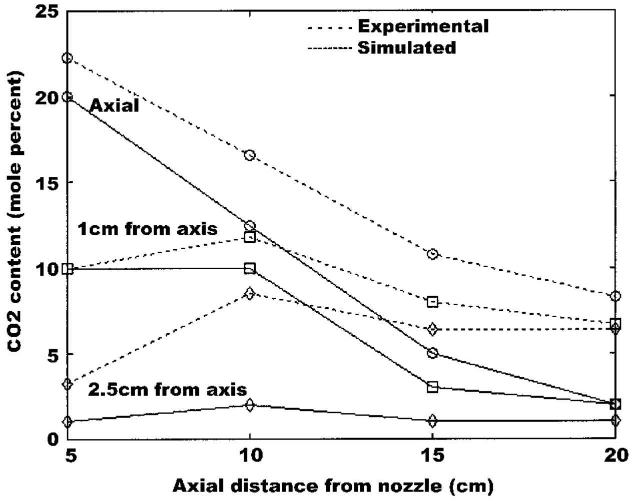

Fig. 7 Predicted and measured CO_2 concentrations

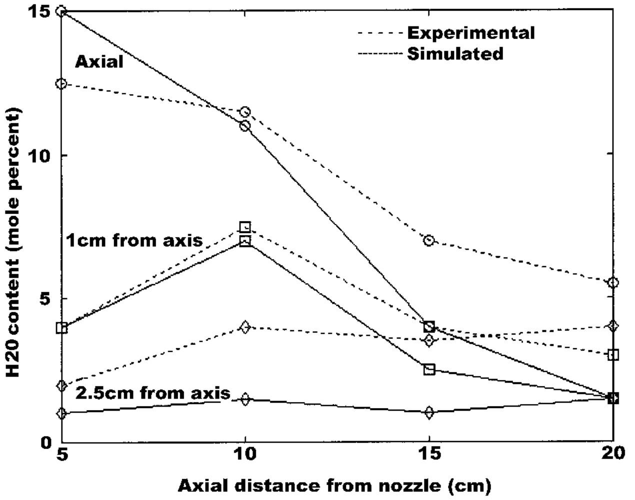

Fig. 8 Predicted and measured H_2O concentrations

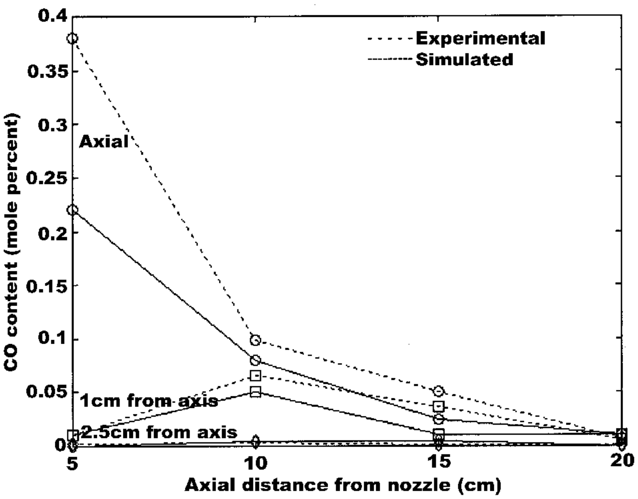

Fig. 9 Predicted and measured CO concentrations

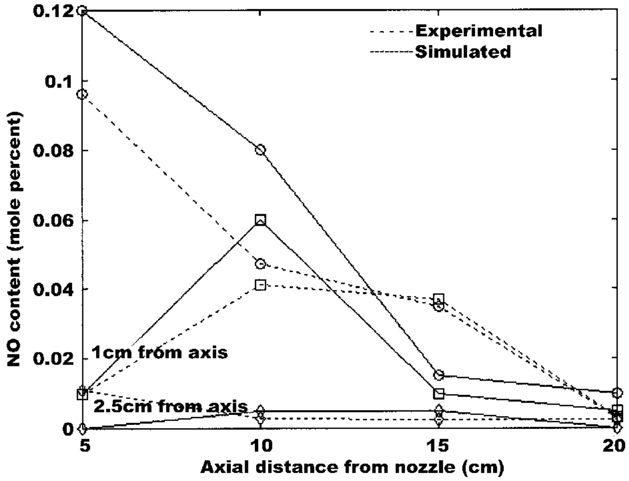

Fig. 10 Predicted and measured NO concentrations

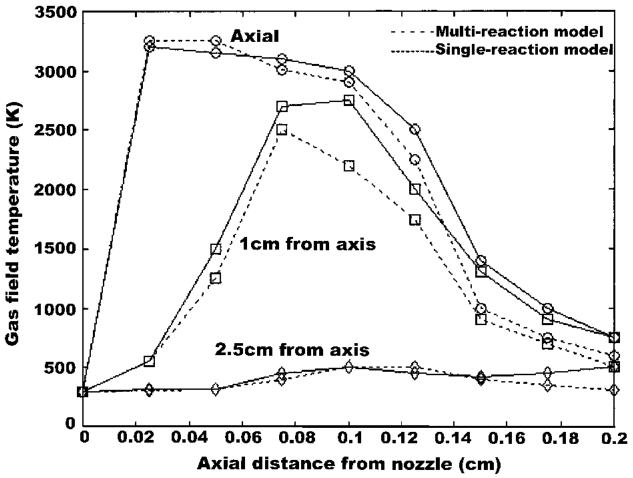

Fig. 11 Comparison of gas field temperature between the multireaction simulation (dashed) and the single-reaction simulation (continuous)

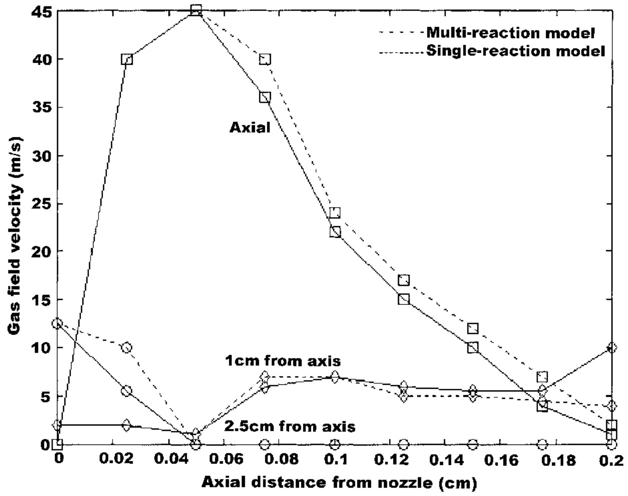

Fig. 12 Comparison of gas velocity between the multireaction simulation (dashed) and the single-reaction simulation (continuous)

7.3 Verification of the Single-Reaction Model: Particle Data Comparisons

The measured particle sizes, velocities, and temperatures of the in-flight sprayed particles presented in this article were taken from available data from previous experimental runs. They were measured using the DPV2000 optical system, produced by Tecnar Automation Ltée (St. Bruno, QC, Canada). The system is based on the detection of thermal radiation from the sprayed particles passing through a control volume via an optical sensor placed close to the spray jet. The images of the particles are formed on a two-slit mask at the end of an optical fiber. The velocity is measured by measuring the time of flight between the two slits, with an accuracy of better than 2%. The temperature is obtained as a gray-body temperature by the use of two-color pyrometry. It can differ from the true temperature if the emissivity at the two wavelengths of measurement is different. The accuracy of the temperature measurement is also dependent on both a calibration procedure and on statistical error. The minimum detectable particle temperature is dependent on the choice of optical filters in front of the photodetectors. For the current measurements it was estimated to be 1600 K for 50 μm particles. This limit applies in the absence of background radiation from gas or particles outside of the control volume reaching the sensor head. Otherwise, the limit is higher. For this reason, the properties had to be measured close to the substrate. The particle diameter is obtained, after calibration, from the radiation collected at one wavelength.

The predicted and measured histograms of the data values are presented in Fig. 13 to 19. It should be remarked that the selected experimental data involves 512 particles passing through the control volume, while the prediction includes 55 injected particle streams scattered over the injection surface, with a size distribution similar to that of the experimental model. The reason for simulating with fewer particles was that the finite difference program used for the calculation of particle characteristics is computation-intensive.

By comparing Fig. 13 and 14, it may be concluded that the size distribution of the particles in the simulated model resembles the size distribution that was experimentally determined. The experimental size distribution shown in Fig. 13 seems to have a lower frequency on the larger diameters and a higher frequency on the 50-80 μm diameters, than the expected distribution (Table 7). The model predicts that the nickel coating has evaporated before reaching this position.

Figure 15 and 16 indicate that the simulated velocity distribution resembles the measured one. The experimental distribution has a pronounced peak at around 22 m/s. The simulated distribution has a somewhat less pronounced peak, but this too also occurs at 22 m/s. The simulated distribution has a wider range than the measured distribution. Furthermore, a small number of particles at velocities exceeding 30 m/s are present in the measurements. A possible explanation for this discrepancy is that interparticle interactions were not included in the current model.

Figure 17 shows the experimental particle temperature distribution, which is to be compared with the predicted distribution in Fig. 18 in which the Lewis expression for the Nusselt number was used, and with Fig. 19 in which the Lee expression was used. Both models predict an evaporation of the nickel.

Neither of the two models displayed the presence of the high temperature particles above 2600 K present in the experimental case. A possible explanation for this could be due to the irregular shape of the particles. The particles in the experiments have a greater surface area, and thereby greater heat absorption. The high temperature values present in the experiments also seem to be somewhat overestimated. Nowhere in the flame was the temperature higher than 3400 K. The values of up to 4000 K present in the measurements are most likely exaggerated. If this is taken into consideration then the predicted and measured values ap-

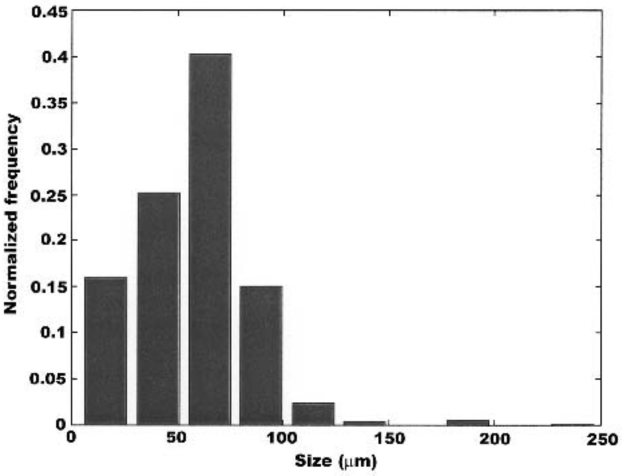

Fig. 13 Measured particle size distribution

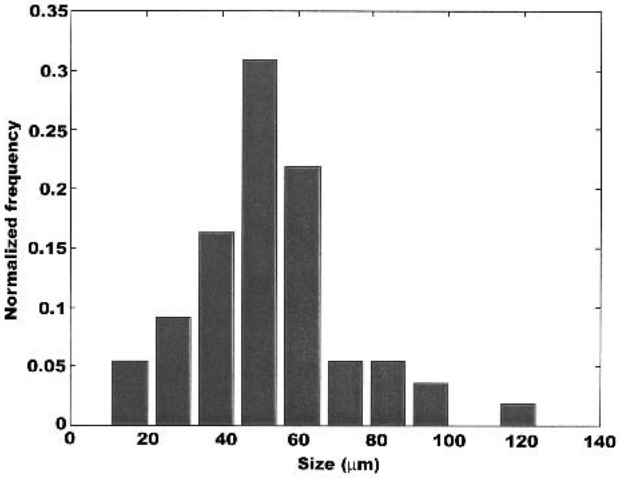

Fig. 14 Predicted particle size distribution

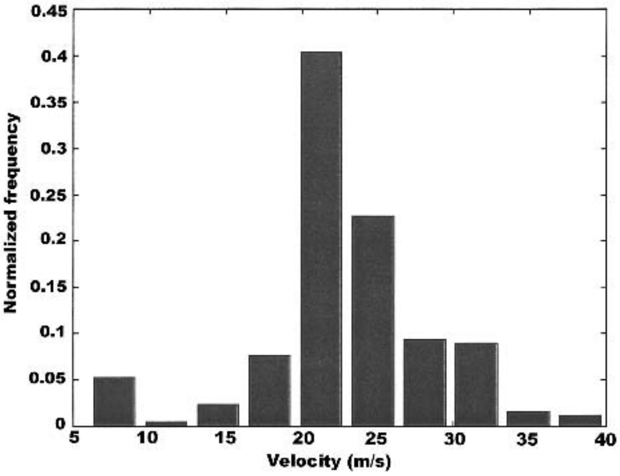

Fig. 15 Measured particle velocity distribution

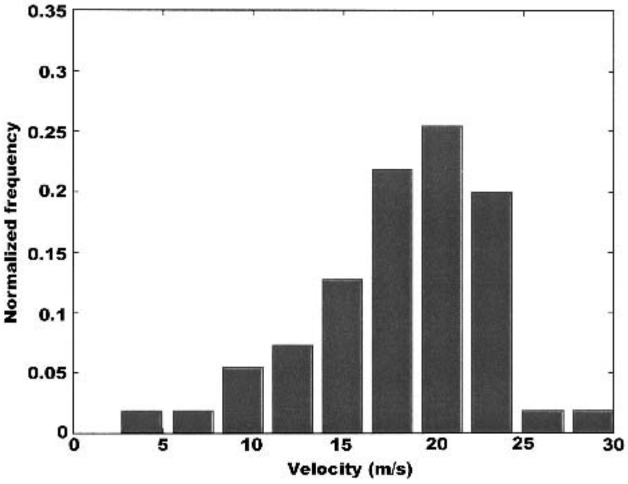

Fig. 16 Predicted particle velocity distribution

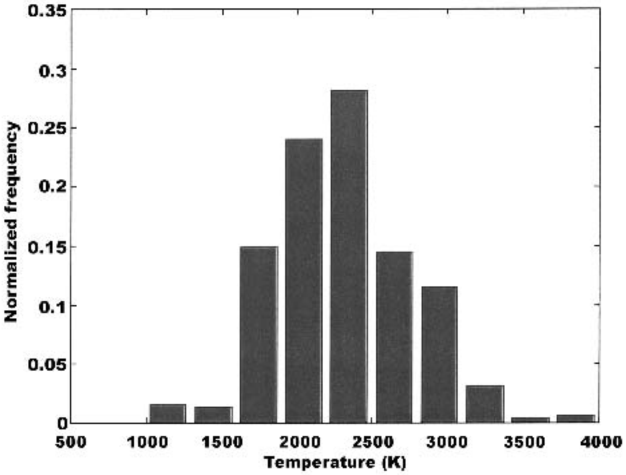

Fig. 17 Measured particle temperature distribution

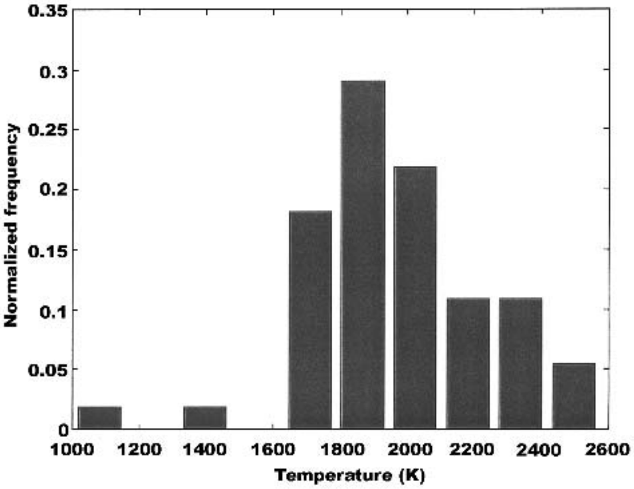

Fig. 18 Predicted particle temperature distribution using the Lewis expression

pear to be more similar. The Lee expression appears to be superior to Lewis expression.

8. Summary and Conclusions

Three-dimensional simulations with full a coupling between the particle and gas flows of a chemically reacting flow in a commercial flame spraying torch have been performed. The first simulations included several intermediate chemical substances whose predicted concentrations agreed favorably with measurements. However, because these simulations were found to be computationally very expensive, a more simple approach, which incorporated only the global chemical reaction, was evaluated. A fairly good agreement in gas velocity and temperature fields between the single-reaction model and the multireaction model was found. Simulations incorporating sprayed particles using

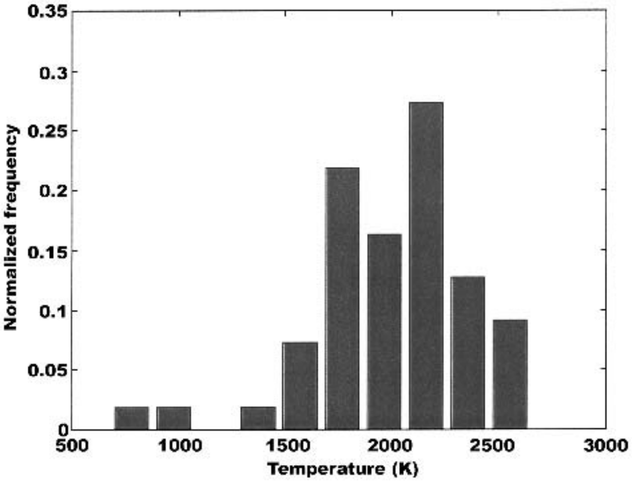

Fig. 19 Predicted particle temperature distribution using the Lee expression

the single-reaction model agreed favorably with corresponding measured particle characteristics. The model presented was considered to be sufficiently successful for studying relationships between varying process parameters and particle in-flight properties. Investigations in this direction are currently being performed.

Acknowledgments

The authors wish to acknowledge the many fruitful discussions with Jan Wigren of the Volvo Aero Corporation and the contribution of Andreas Boklund at the University of Trollhättan/Uddevalla for the construction of the computer cluster that made these computations possible. This project has been kindly funded by the Foundation for Knowledge and Competence Development and by EC Structural Founds.

References

1. E.B. Smith, G.D. Power, T.J. Barber, and L.M. Chiappetta: "Applications of Computational Fluid Dynamics of the HVOF Thermal Spray Torch" in *Thermal Spray: International Advances in Coatings Technology,* C.C. Berndt, ed., ASM International, Materials Park, OH, 1992, pp. 805-10.
2. X.Yang, S. Eidelman, and I. Lottati: "Numerical Simulation of Gas and Particle Flow Field Characteristics in HVOF Torches" in *Advances in Thermal Spray Science and Technology,* C.C. Berndt and S. Sampath, ed., ASM International, Materials Park, OH, 1995, pp. 213-18.
3. W.L. Oberkampf and M. Talpallikar: "Analysis of a High Velocity Oxygen-Fuel (HVOF) Thermal Spray Torch, Part 1: Numerical Formulation" in *Thermal Spray Industrial Applications,* C.C. Berndt and S. Sampath, ed., ASM International, Materials Park, OH, 1994, pp. 381-86.
4. B. Hassan, A.R. Lopez, and W.L. Oberkampf: "Computational Analysis of a Three-Dimensional High-Velocity Oxygen-Fuel (HVOF) Thermal Spray Torch" in *Advances in Thermal Spray Science and Technology,* C.C. Berndt and S. Sampath, ed., ASM International, Materials Park, OH, 1995, pp. 193-98.
5. A.R. Lopez, B. Hassan, W.L. Oberkampf, R.A.Neiser, T.J. Roemer: "Computational Fluid Dynamics Analysis of a Wire-Feed, High-Velocity Oxygen-Fuel (HVOF) Thermal Spray Torch" in *Thermal Spray: Practical Solutions for Engineering Problems,* C.C. Berndt, ed., ASM International, Materials Park, OH, 1996, pp. 531-40.

6. C.H. Chang and R.L. Moore: "Simulation of Gas Particle Flow in a HVOF Torch," *Proceedings of NTSC 1995,* C.C. Berndt and S. Sampath, ed. ASM International, Materials Park, OH, pp. 207-12.
7. C.H. Chang and R.L. Moore: "Numerical Simulation of Gas and Particle Flow in a HVOF Torch," *J. Thermal Spray Technol.*, 1995, *4,* pp. 358-66.
8. J.C. Mackie and J.C. Smith: "Inhibition of C_2 Oxidation by Methane Under Oxidative Coupling Conditions," *Energy & Fuels*, 1990, *4*(3), pp. 277-85.
9. M.W. Chase, C.A. Davies, J.R. Downey, D.J. Frurip, et al: *JANAF Thermodynamical Tables,* 3rd ed., American Chemical Society, Washington, DC, American Institute of Physics for the National Bureau of Standards, New York, NY, 1986.
10. M.I. Boulos: *Thermal Plasmas, Fundamentals and Applications,* Vol. 1, Plenum Press, New York, NY, 1994.
11. J. Wigren, M.O. Hansson, P. Gougeon, and C. Moreau: "On-Line Diagnostics of Traditional Flame Spraying as a Tool to Increase Reproducibility" in *Thermal Spray: Practical Solutions for Engineering Problems,* C.C. Berndt, ed., ASM International, Materials Park, OH, 1996, pp. 675-81.
12. W.E. Ranz and W.R. Marshall: "Evaporation from Drop, Part I", *Chem. Eng. Progr.,* 1952, *48,* p. 141.
13. Y.C. Lee, Y.C. Chyou, and E. Pfender: "Particle Dynamics and Particle Heat and Mass Transfer in Thermal Plasmas. Part II," *Plasma Chem. Plasma Proc.,* 1985, *5,* pp. 391-414.
14. J.A. Lewis and W.H. Gauvin: "Motion of Particles Entrained in a Plasmas Jet," *AJChE J.,* 1978, *19*(5), pp. 982-90.
15. L.V. Gurvich, I.V. Vetys, and C.B. Alcock: *Thermodynamic Properties of Individual Substances,* Hemisphere Press, New York, NY, 1996.